Influence of the rare earth concentration on the crystallization process of Fe-Dy-B amorphous alloys. Study of $Fe_{74}Dy_6B_{20}$ and $Fe_{70}Dy_{10}B_{20}$ alloys

2000 J. Phys.: Condens. Matter 12 3639

(http://iopscience.iop.org/0953-8984/12/15/313)

J. Phys.: Condens. Matter **12** (2000) 3639–3660. Printed in the UK PII: S0953-8984(00)09087-1

Influence of the rare earth concentration on the crystallization process of Fe–Dy–B amorphous alloys. Study of $Fe_{74}Dy_6B_{20}$ and $Fe_{70}Dy_{10}B_{20}$ alloys

G Ravach†, F Machizaud‡, J Teillet†, J M Le Breton† and A Fnidiki†

† GMP, Magnétisme et Applications, UMR CNRS 6634, Université de Rouen, F-76821 Mont-Saint-Aignan Cédex, France

‡ LSG2M, Ecole des Mines de Nancy, UMR CNRS 7584, Parc de Saurupt, F-54042 Nancy Cédex, France

Received 29 October 1999, in final form 20 January 2000

Abstract. The crystallization behaviour of $Fe_{74}Dy_6B_{20}$ and $Fe_{70}Dy_{10}B_{20}$ amorphous alloys was carefully investigated by differential scanning calorimetry, Mössbauer spectrometry and x-ray diffraction up to 800 °C. Calorimetric studies were performed in limited temperature ranges that were progressively extended. For $Fe_{74}Dy_6B_{20}$, after partial crystallization into the tetragonal Fe_3B compound, the remaining amorphous part segregates into two amorphous 'phases', respectively enriched and impoverished in dysprosium. Tetragonal Fe_3B further transforms into orthorhombic Fe_3B. Metastable $Dy_3Fe_{62}B_{14}$ compound then forms from the Dy-impoverished amorphous fraction, and subsequent crystallization of the $Dy_{1+\varepsilon}Fe_4B_4$ phase occurs in the Dy-enriched fraction. Finally, $Dy_3Fe_{62}B_{14}$ decomposes into bcc iron, $Dy_{1+\varepsilon}Fe_4B_4$ and iron borides. The nature of the first crystallization product suggests the existence of local environments of t-Fe_3B type for this Dy concentration. The crystallization process of $Fe_{70}Dy_{10}B_{20}$ strongly differs from that of $Fe_{74}Dy_6B_{20}$. Segregation phenomena occur in the amorphous state prior to any crystallization. If the nature of the first crystallization product is assumed to be correlated with short-range order in the amorphous state, our results suggest that the local environments differ from those of $Fe_{74}Dy_6B_{20}$, as they probably involve dysprosium atoms. This behaviour would agree with a previous Mössbauer study performed on the as-quenched amorphous alloys, providing evidence for a structural modification of the iron environments in the rare earth concentration range 8–9 at.%.

1. Introduction

In the last decade, quite numerous magnetic studies were dedicated to ternary amorphous systems containing transition metal (TM), rare earth (R) and metalloid elements (Me), particularly with compositions such as $TM_{80-x}R_xMe_{20}$ [1]. As the distribution of local easy magnetization axes over the various atomic sites results from the combination of topological disorder, which induces a distribution of atomic environments, and spin–orbit coupling, the understanding of the random magnetic anisotropy properties of these materials requires a precise knowledge of their local structural features. We recently investigated the Mössbauer behaviour of melt-spun $Fe_{80-x}R_xB_{20}$ amorphous ribbons ($x \leqslant 16$ at.%; R = Dy, Ho, Nd) as a function of the concentration and the nature of the rare earth [2–4]. We provided evidence for a drastic discontinuity in the variation of the mean hyperfine parameters with the rare earth concentration, occurring around $x = 8$–9 at.% whatever the nature of the rare earth atom. We attributed this discontinuity to a strong modification in local order around Fe atoms in this

0953-8984/00/153639+22$30.00

composition range. However, further investigation was necessary to identify precisely the type of local order below and beyond the critical concentration x_c.

Among the various ways to characterize amorphous materials, the study of their crystallization processes revealed itself successful in determining pre-existing structural features of the amorphous state as shown for amorphous $Fe_{100-x}B_x$ alloys ($12 < x \leqslant 25$ at.%) [5–7]. This indirect approach goes on the assumption of a correlation between short-range order in the amorphous state and the nature of the first crystallization products. In $Fe_{100-x}B_x$ alloys ($x = 20$, 25 at.%), the first crystallization product was identified as tetragonal Fe_3B (t-Fe_3B) [5–9]. Following this idea, we undertook a comparative crystallization study of our alloys on both sides of the critical concentration x_c established by Mössbauer experiments. In the present paper, we report on the investigation of the crystallization process for two amorphous alloys, with rare earth concentration lying below ($Fe_{74}Dy_6B_{20}$) and beyond ($Fe_{70}Dy_{10}B_{20}$) the critical concentration x_c.

2. Experiment

Ingots of nominal composition $Fe_{74}Dy_6B_{20}$ and $Fe_{70}Dy_{10}B_{20}$ were prepared by induction melting from elements of purity higher than 99.9% (99.99% in the case of iron). Melting was performed under an inert atmosphere of argon to prevent the oxidation of dysprosium. In order to limit the preferential rare earth evaporation generally observed during melting [10], the ingot was prepared in two stages. The first one consisted in the elaboration of an Fe–B alloy with a composition close to the deep eutectic in the binary phase diagram (melting point about 1250 °C). Ribbons were then obtained from the ingot by the usual melt-spinning technique, under an argon flow. The ejection of the melt alloy was performed on a copper wheel with tangential velocity of 35 m s^{-1}, under a helium pressure of 4×10^4 Pa. The composition of the ribbons was determined by electron probe microanalysis. The measured dysprosium contents were 5.4 at.% and 9.5 at.% respectively, slightly lower than the nominal concentration. For simplicity, the alloys will be referred to by their nominal composition in the following.

Thermal treatments were performed under an inert atmosphere of argon by differential scanning calorimetry (SETARAM DSC 111 apparatus), with a constant heating rate of 5 °C min^{-1} and further with a mean cooling rate of 25 °C min^{-1} to room temperature. For these treatments, ribbons were crushed to powder and sieved to a particle size between 25 and 40 μm. The materials were characterized at room temperature by x-ray diffraction (XRD) using Co ($K\alpha_1$) radiation, and ^{57}Fe transmission Mössbauer spectrometry (MS), before and after various thermal treatments. MS experiments were carried out with a source of ^{57}Co in a rhodium matrix. The spectra were computer fitted with a least-squares technique [11]. For amorphous spectra, we used the histogram method relative to discrete distributions of single crystals [12], constraining the linewidth Γ of each elementary sextet to be the same. The asymmetry of amorphous spectra was accounted for by a linear correlation between isomer shifts IS and hyperfine fields B_{hf}. The mean values of isomer shift $\langle IS \rangle$ are given relative to α-Fe at room temperature.

3. Characterization of the materials before thermal treatments

3.1. As-quenched ribbons

As-quenched ribbons were analysed by XRD and MS to characterize their amorphous state. Mössbauer results are presented elsewhere [3] and this section deals with XRD measurements. The sample thickness (typically 30 μm) allowed a selective XRD study of the two ribbon

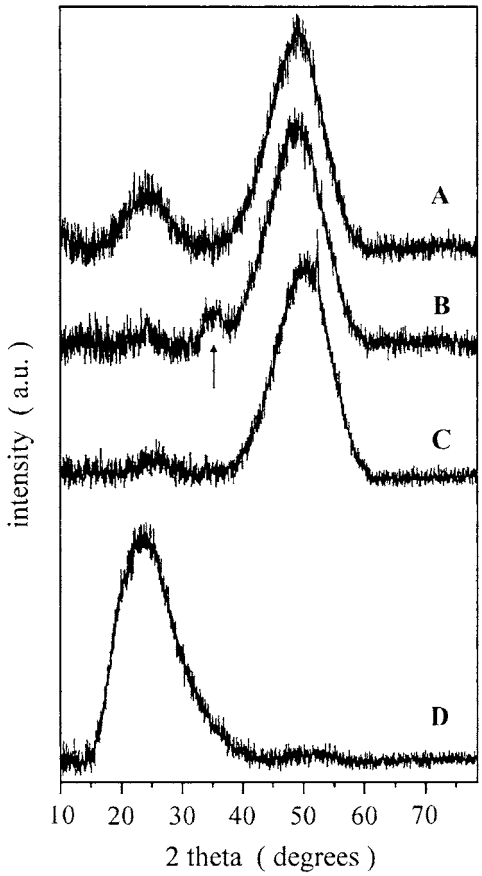

Figure 1. Room temperature XRD patterns of $Fe_{74}Dy_6B_{20}$ alloy: (A) ribbon wheel side; (B) ribbon free side; (C) powder; (D) sample holder.

sides, solidified respectively in contact with the copper wheel (wheel side) and in ambient argon atmosphere (free side).

For $Fe_{74}Dy_6B_{20}$, the XRD patterns are typical for amorphous materials, whatever the side (figure 1(A), (B)). The maximum observed around $2\theta = 25^\circ$ is due to the contribution of the sample holder, as evidenced by its XRD pattern (figure 1(D)). The wheel side pattern exhibits a large and slightly asymmetrical maximum at $2\theta = 50^\circ$ (figure 1(A)), representative of mean interatomic distances of 0.26 nm mainly corresponding to the Fe–Fe correlations. The position and width of this main contribution are identical on the free side of the ribbons (figure 1(B)). The main difference between the two sides lies in the presence of a broad maximum at $2\theta \approx 35^\circ$ in the case of the free side. It corresponds to mean interatomic distances close to the dysprosium atomic diameter (0.36 nm), and reveals the existence of Dy–Dy correlations. They were attributed to a rare earth oxide forming tendency as, first, the argon atmosphere may not be totally oxygen free and, second, the lower quenching rate favours atomic arrangements on the free side.

The diffraction pattern of $Fe_{70}Dy_{10}B_{20}$ exhibits strong similarities with those of $Fe_{74}Dy_6B_{20}$ alloy. The mean interatomic distance (0.27 nm in $Fe_{70}Dy_{10}B_{20}$) is slightly higher than in $Fe_{74}Dy_6B_{20}$ (0.26 nm), owing to the size effect of dysprosium atoms. As was the case

for the lower dysprosium concentration, our XRD analyses reveal the existence of Dy–Dy correlations, especially on the free side of the ribbons.

3.2. Effect of ribbon powdering

The features of the XRD pattern of the powdered alloy (figure 1(C)) are close to those of the ribbon wheel side (A), confirming that Dy–Dy correlations are mostly localized on the free side. Although the powdered alloy is essentially amorphous, a sharp line is observed at $2\theta \approx 52^\circ$, corresponding to a d-spacing of 0.2024 nm. It was attributed to the (110) line of bcc iron ($d_{110} = 0.202\,68$ nm, but this crystallization of bcc iron is not detected by Mössbauer analysis of the powder (phase detectability threshold (1–2%)). However, for transmission Mössbauer spectrometry, we studied the powder particles as a whole, while for XRD, 95% of the measured intensity is diffracted by a surface layer of about 5 μm in depth (after [13]). The apparent discrepancy between the results can then be understood if the bcc iron crystallites are mainly localized at the surface of the particles. This suggests that the iron crystallization is induced by local overheating and/or stresses resulting from the friction between the particles on powdering. This effect is very weak and does not modify significantly the characteristics of the remaining amorphous fraction, as shown by XRD and MS. However, such ordered regions may constitute favourable sites for the precipitation of crystalline phases during the thermal treatments.

Some crystallization of bcc iron is also observed in $Fe_{70}Dy_{10}B_{20}$ by XRD when the alloy is powdered.

4. Crystallization of $Fe_{74}Dy_6B_{20}$

4.1. Calorimetric investigation

4.1.1. Heating up to 800 °C. A sample of powdered $Fe_{74}Dy_6B_{20}$ alloy was first heated from room temperature (RT) up to 800 °C and then cooled down to room temperature and heated again up to 800 °C. The DSC curve recorded on the first heating exhibits three sharp exothermic peaks with maxima at 622 °C (P_1), 658 °C (P_2) and 733 °C (P_3) respectively (figure 2(a)). P_1 and P_3 are preceded by two wide maxima of weaker intensity at 589 °C (M_1) and 697 °C (M_2). Other weak variations are observed at lower temperatures on the curve but their identification as exo- or endothermic reactions is rather a difficult task owing to the choice of a suitable baseline for the DSC curve. Usually, one takes as the baseline the DSC curve obtained for the same sample, during a second identical heating carried out in similar operating conditions and immediately after the first thermal treatment. However, in such a large temperature range, important structural transformations occur in the alloy, as it evolves from a metastable amorphous state to a stable crystalline one. In order to obtain more reliable information about the calorimetric behaviour of our alloy, we performed successive treatments on a same sample, in much reduced temperature ranges that were progressively extended and we analysed the two 'as-recorded' DSC curves, without any correction.

4.1.2. Successive treatments. Two series of treatments performed on two samples (A and B) will be detailed as they give complementary results.

The successive treatments performed on sample A, and the corresponding DSC curves, are detailed in figure 3. The two DSC curves (a) and (b) were obtained when the temperature was raised up to 350 °C. Curve (b) shows a wide minimum at 257 °C corresponding to the Curie temperature T_C^{am} of the as-quenched ribbons determined from magnetization measurements

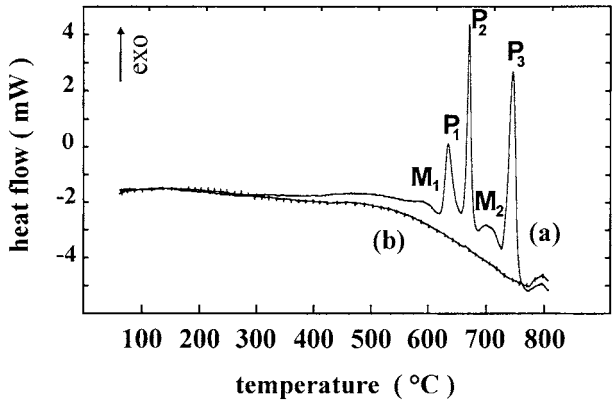

Figure 2. DSC curves of $Fe_{74}Dy_6B_{20}$ up to 800 °C, with a heating rate of 5 °C min^{-1}. Curve (a) is relative to the first heating, curve (b) to the second heating stage.

[14]. This magnetic transition has a weak amplitude and spreads over a large temperature range as already observed in amorphous $Fe_{80.3}Ho_{1.7}B_{18}$ alloy [15]. As shown on the DSC curve (a), an irreversible exothermic reaction (E_1) occurs in this temperature range on the first heating stage. It is attributed to a structural relaxation of the material and the corresponding enthalpy variation $\Delta H(E_1)$, estimated as 1.3 kJ mol^{-1} from the area delimited by curves (a) and (b), is typical of structural relaxation in most metallic amorphous alloys ($\approx$1 kJ mol^{-1} [16]). Curves (c) and (d) correspond to further heatings up to 550 °C, that is below the reaction M_1 in figure 2. As expected, the magnetic transition T_C^{am} is still observed on curve (c). The minimum T_C^1 observed at the limit of the explored range is located at 535 °C, close to the Curie temperature of the tetragonal Fe_3B compound (t-Fe_3B) (527–547 °C [17]). t-Fe_3B may have been formed during the exothermic reaction (E_2) observed around 450 °C on curve (c). In our alloy, the concentration ratio Fe/B is close to that of $Fe_{79}B_{21}$, that crystallizes into bcc iron and Fe_3B by eutectic reaction [9]. For a scanning rate of 5 °C min^{-1}, the crystallization temperature of this binary alloy is about 440 °C [9], which corresponds to the temperature range characteristic of E_2. As low rare earth contents are known to enhance crystallization temperatures in Fe–B amorphous alloys ([15] and references therein), it is excluded that t-Fe_3B forms during the reaction E_1. The formation of t-Fe_3B is at the origin of structural modifications in the remaining amorphous fraction, leading to a 20 °C increase of its Curie temperature T_C^{am} as observed on curve (d). The enthalpy variation $\Delta H(E_2)$ was estimated as 2.4 kJ mol^{-1}. Sample A was next heated up to 673 °C, just above the reaction P_2 (figure 3(e)). The magnetic transition of the amorphous fraction, which occurs at T_C^{am} during the first treatment, is no longer observed on the second curve (f), indicating the complete transformation of the remaining amorphous fraction. On heating up to 800 °C, the last two exothermic reactions (M_2 and P_3) occur, as shown on the curve (g). A minimum T_C^2 is observed at about 640 °C, that can be attributed to the Curie transition of the orthorhombic Fe_3B compound (627 °C [18]). This transition is already observed on curve (f), and the compound is formed at the latest on the occurrence of P_2. As curve (h) shows this minimum as well, o-Fe_3B is one of the final crystallization products. Curve (h) exhibits another minimum at 765 °C, that can be attributed to the magnetic transition T_C^4 of bcc iron (771 °C [19]). The minimum of very weak intensity at 710 °C might correspond to the magnetic transition T_C^3 of the Fe_2B compound (742 °C [20]). Although their intensity is very weak, the minima T_C^2 , T_C^3 and T_C^4 are significant. The presence of o-Fe_3B, Fe_2B and bcc iron will be confirmed by both x-ray diffraction and Mössbauer analyses.

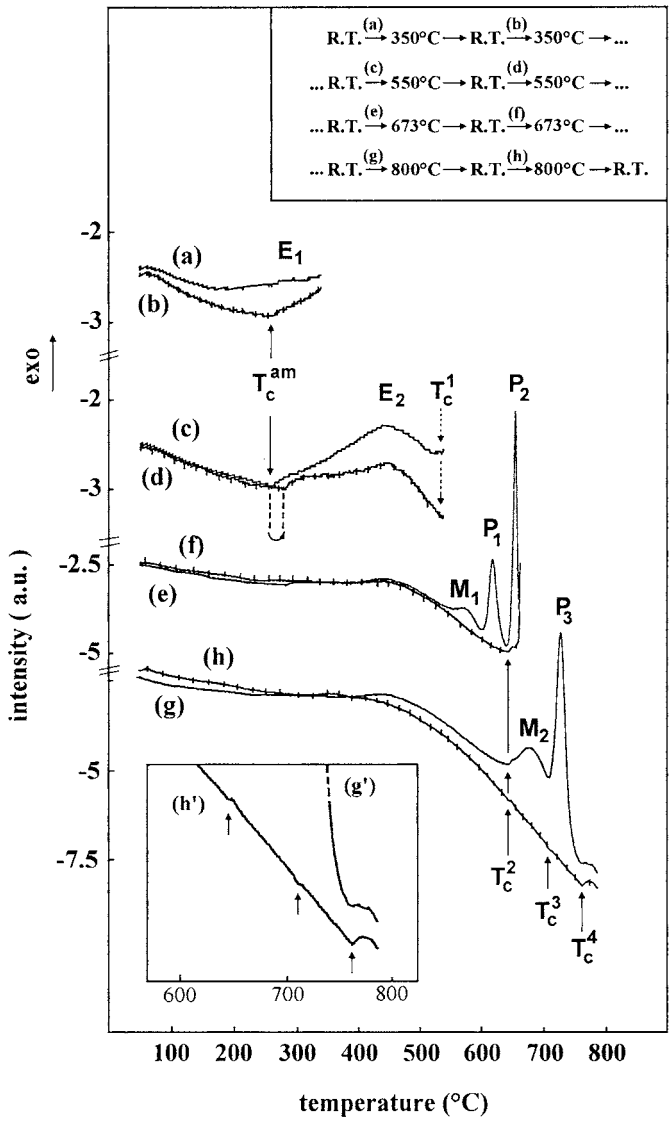

Figure 3. DSC scans obtained for successive thermal treatments on sample A. (g′) and (h′): expanded view of curves (g) and (h) in the temperature range 600–800 °C.

Sample B was first heated up to 605 °C, a temperature which is just above M_1. The presence of t-Fe_3B is confirmed through its magnetic transition occurring at T_C^1 (figure 4(a)). The first heating leads here again to an increase of the Curie temperature T_C^{am} of the amorphous alloy when treated again (figure 4(b)). It is much more important than the one induced by E_2 in sample A (about 50 °C), indicating that M_1 is responsible for further structural changes in the amorphous alloy. As the Curie transition of t-Fe_3B is no longer observed on curve (b), this metastable compound disappears on the occurrence of M_1. An additional heating up to 715 °C (curve d) should not induce the P_3 phenomenon observed in figure 2. However, the DSC curve displayed in figure 4(c) shows that P_3 has been initiated, indicating that previous thermal

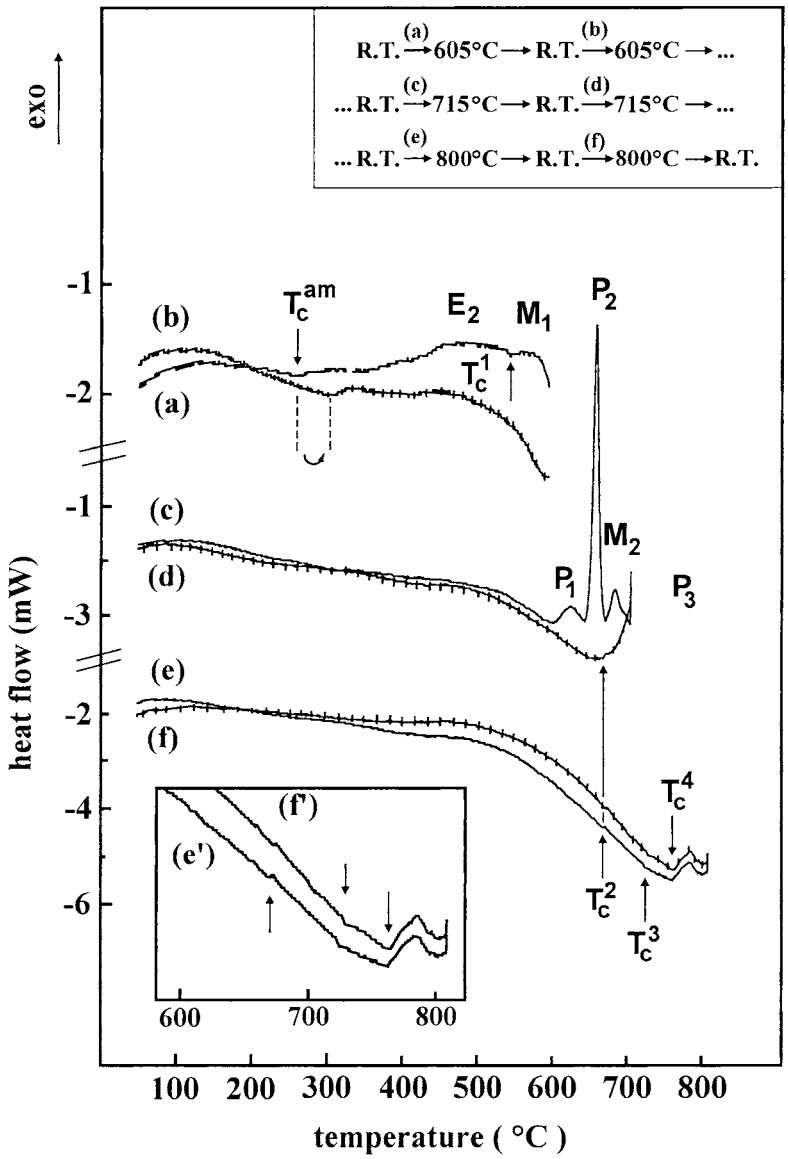

Figure 4. DSC scans obtained for successive thermal treatments on sample B. (e′) and (f′): expanded view of curves (e) and (f) in the temperature range 600–800 °C.

treatments shifted the reaction onset towards lower temperatures. The reaction does not take place on further heating up to 800 °C (figure 4(e)), confirming that P_3, initiated at 715 °C, was completed on the last cooling from 715 °C to RT. The strong decrease of P_1 intensity observed on curve (c) suggests that this reaction partially occurred on previous treatments up to 605 °C. The absence of P_1 on curves (a) and (b) shows that this reaction, probably initiated by M_1, went on cooling. In agreement with the results obtained for sample A, curve (d) displays the minimum T_C^2 characteristic of the Curie transition of o-Fe_3B. The magnetic transitions of o-Fe_3B, Fe_2B and bcc iron, observed on curves (d) and (e), confirm the presence of those compounds as final crystallization products.

4.2. Characterization of the crystallization products

Further characterization of the crystallization products was performed by XRD and MS on various samples heated once up to temperatures T_m corresponding to the maxima of the exothermic reactions P_1 (623 °C), P_2 (659 °C), M_2 (695 °C) and P_3 (732 °C) and to the final temperature (800 °C). The thermal treatments were carried out in the same operating conditions as in the calorimetric study.

4.2.1. XRD measurements (figure 5). At 623 °C, the XRD pattern consists of two broad maxima at $2\theta = 25°$ (sample holder) and $2\theta = 50°$ (remaining amorphous fraction), already observed in figure 1, and a set of sharp lines. As intensities of bcc iron(110) and (200) lines seem unchanged, the iron crystallites formed on powdering did not grow in the temperature range $T \leqslant 623$ °C. Most of the sharp lines can be attributed to a metastable $Dy_3Fe_{62}B_{14}$ body-centred cubic phase with a $Y_3Fe_{62}B_{14}$-type structure [21]. The measured lattice parameter $a = 1.234 \pm 0.001$ nm is in good agreement with the value given for $Dy_3(Fe, Nb)_{62}B_{14}$ (1.235 nm [22]). Only two lines cannot be explained by the presence of bcc iron and $Dy_3Fe_{62}B_{14}$. They are weak, but their positions correspond to the (111) and (201) lines of the o-Fe_3B compound [23]. The other lines of o-Fe_3B are strongly convoluted with those of $Dy_3Fe_{62}B_{14}$. It must be added that the presence of t-Fe_3B cannot explain these two lines, but its d-spacings [24] are included in our experimental data, and the presence of t-Fe_3B cannot be excluded *a priori*.

Between 623 and 659 °C, further crystallization of the remaining amorphous fraction is observed, but no new crystalline phase is formed. The proportion of $Dy_3Fe_{62}B_{14}$ increases relative to those of bcc iron and o-Fe_3B. At 695 °C, the lines of the $Dy_3Fe_{62}B_{14}$ compound are still observed. All the new maxima appearing at this temperature can be attributed to the crystallization of $Dy_{1+\varepsilon}Fe_4B_4$ phase, the experimental d-spacings agreeing within 0.001 nm accuracy with the values calculated after [25] using the lattice parameters published for $Dy_{1.152}Fe_4B_4$ [26]. Those maxima are poorly defined, suggesting the small size of the crystallites. The formation of $Dy_{1+\varepsilon}Fe_4B_4$ phase is confirmed at 732 °C (P_3). The intensity of bcc-iron lines strongly increases while the lines of $Dy_3Fe_{62}B_{14}$ are much reduced. Only one line cannot be attributed to bcc iron, $Dy_{1+\varepsilon}Fe_4B_4$ or $Dy_3Fe_{62}B_{14}$. It might correspond to the (130) line of Fe_2B boride ($d_{130} = 0.161\,66$ nm [27]). For this compound, the other lines are common with some of bcc iron and $Dy_3Fe_{62}B_{14}$, and the Fe_2B boride might be present as traces. As at 695 °C, the presence of o-Fe_3B is most probable. The lines of $Dy_3Fe_{62}B_{14}$ have totally disappeared at 800 °C. bcc iron and $Dy_{1+\varepsilon}Fe_4B_4$ are the major phases in the alloy and traces of Fe_2B boride are detected. Other weak lines can be seen on the pattern. Two of them can be attributed to o-Fe_3B, the other lines of this system being still convoluted with those of other phases. The remaining lines, which could not be identified rigourously, might be related to traces of dysprosium oxides.

4.2.2. Mössbauer results. Mössbauer spectra corresponding to the five samples previously studied by XRD are compared with the untreated powder spectrum in figure 6. Except for $Dy_3Fe_{62}B_{14}$, the room temperature hyperfine parameters of the different crystalline phases observed by DSC and XRD are available in the literature [26, 28–31]. First, in agreement with the XRD study, the Mössbauer spectrum of the sample heated up to 800 °C (figure 6(E)) was fitted with four contributions, in order to account for the two iron sites present in o-Fe_3B, and for the iron site in bcc iron and $Dy_{1+\varepsilon}Fe_4B_4$, constraining the same linewidth value $\Gamma = 0.29$ mm s^{-1}. The fitted hyperfine parameters, given in table 1, agree with those of bcc iron, $Dy_{1+\varepsilon}Fe_4B_4$ and o-Fe_3B within experimental accuracy. The intensity ratio of the two

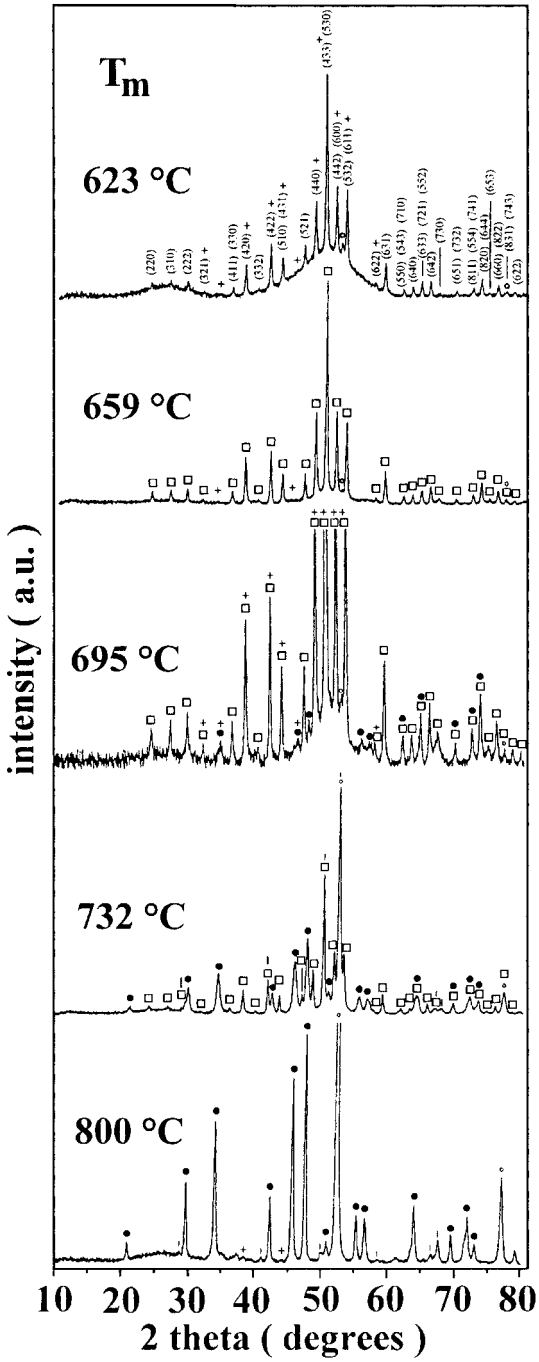

Figure 5. Room temperature XRD patterns of $Fe_{74}Dy_6B_{20}$ after thermal treatments up to T_m. (*hkl*) and (□): $Dy_3Fe_{62}B_{14}$; (+): o-Fe_3B; (○): bcc iron; (●): $Dy_{1+\varepsilon}Fe_4B_4$; (|): Fe_2B.

o-Fe_3B iron sites (1/2.1) corresponds to the theoretical value (1/2), confirming the presence of the boride. Another fit was performed, adding a fifth component in order to account for

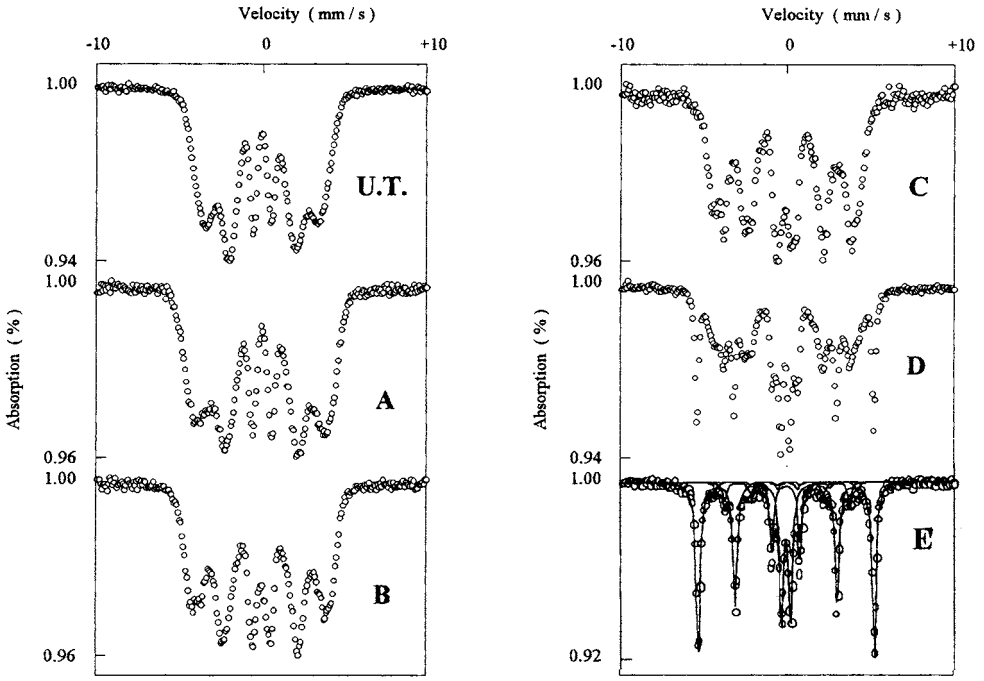

Figure 6. Room temperature Mössbauer spectra of $Fe_{74}Dy_6B_{20}$: untreated powder (U.T.) and after thermal treatments up to 623 °C (A), 659 °C (B), 695 °C (C), 732 °C (D) and 800 °C (E).

Fe_2B, but the experimental intensity ratios do not agree with the theoretical site occupancies for iron borides, confirming that Fe_2B can only be present as traces. At 732 °C, the spectrum (figure 6(D)) is a mixture of bcc iron, $Dy_{1+\varepsilon}Fe_4B_4$, $Dy_3Fe_{62}B_{14}$ and iron borides (mainly o-Fe_3B). Owing to the lack of Mössbauer data for $Dy_3Fe_{62}B_{14}$, the spectrum could not be fitted in totality. However, from a partial fitting of the data (figure 7(D′)), the bcc iron and $Dy_{1+\varepsilon}Fe_4B_4$ Mössbauer abundances were estimated as 34.1 and 19.3% respectively. The spectrum displayed in figure 7(D″), obtained by subtracting the calculated contributions to the experimental data, is close to the spectrum recorded after a heating up to 695 °C (figure 6(C)). The spectra obtained at 623 °C (figure 6(A)) and 659 °C (figure 6(B)) look like amorphous spectra, although XRD showed that they both contain crystalline $Dy_3Fe_{62}B_{14}$ and o-Fe_3B, added to an amorphous fraction. The crystalline fraction is more important at 659 °C. Accounting for the shape of the spectra and the numerous parameters, the data were fitted with a distribution of hyperfine parameters (figure 8). A paramagnetic component with Mössbauer abundance of about 9% (table 2) has to be considered to account for the enhancement of the central line intensity at 659 °C (figure 8(B)). The hyperfine parameters of this paramagnetic contribution (table 2) agree with those of $Dy_{1+\varepsilon}Fe_4B_4$ within experimental accuracy. Accounting for its important linewidth Γ, this contribution seems disordered, and might correspond to an amorphous precursor of the crystalline phase $Dy_{1+\varepsilon}Fe_4B_4$.

4.3. Discussion

The first stage observed during the thermal treatments of $Fe_{74}Dy_6B_{20}$ alloy is a structural relaxation (E_1) of the amorphous state, occurring around 250 °C. As usual in binary $Fe_{80}B_{20}$

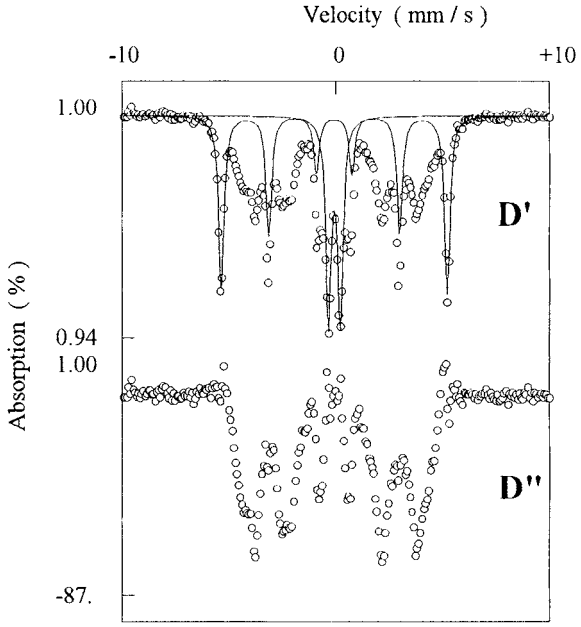

Figure 7. Partial fitting of the Mössbauer spectrum of $Fe_{74}Dy_6B_{20}$ after a thermal treatment up to 732 °C (D′). (D″): unfitted remaining contribution.

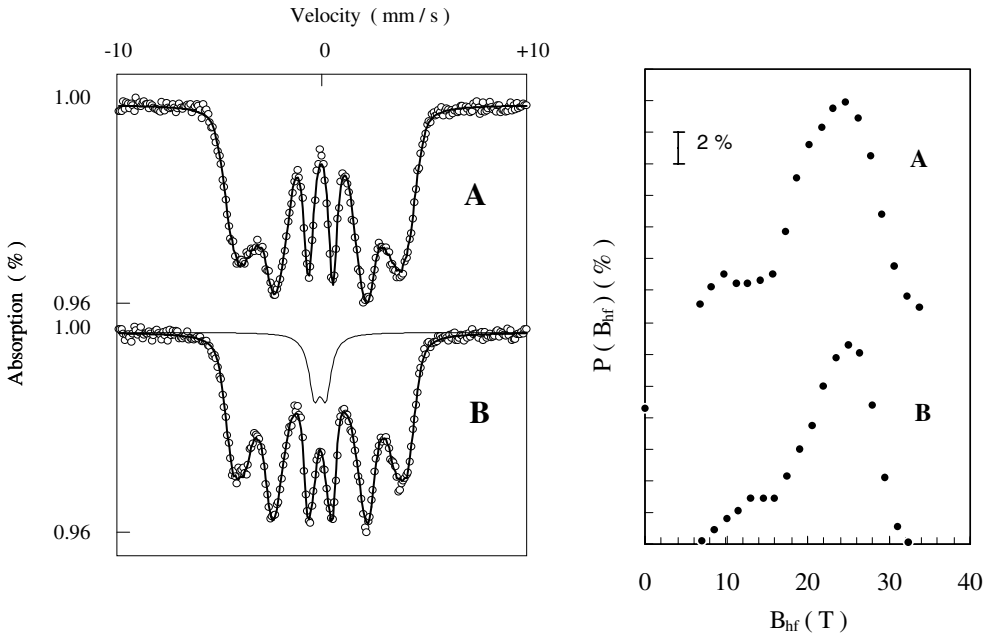

Figure 8. Fittings of the Mössbauer spectra of $Fe_{74}Dy_6B_{20}$ after thermal treatments up to 623 °C (A) and 659 °C (B) and corresponding hyperfine field distributions. The extra paramagnetic component is displayed.

amorphous alloy [32], no significant effect on the Curie temperature is observed after structural relaxation. Subsequently, we observe an exothermic reaction E_2 at 450 °C, associated with the

Table 1. Room temperature hyperfine parameters of $Fe_{74}Dy_6B_{20}$ components after a treatment up to 800 °C.

Component	B_{hf} (T)	IS (mm s^{-1})	QS or 2ε (mm s^{-1})	Abundance (%)
bcc iron	32.8 ± 0.2	0.002 ± 0.003	0	66
$Dy_{1+\varepsilon}Fe_4B_4$	0	0.013 ± 0.005	0.54 ± 0.01	24
o-Fe_3B	26.4 ± 0.5	0.10 ± 0.07	-0.1 ± 0.1	3
	23.2 ± 0.2	0.09 ± 0.03	-0.02 ± 0.06	7

Table 2. Mean hyperfine parameters deduced from the fittings of $Fe_{74}Dy_6B_{20}$ Mössbauer spectra after treatments up to 623 °C and 659 °C.

Component	B_{hf} (T)	IS (mm s^{-1})	QS or 2ε (mm s^{-1})	Γ (mm s^{-1})	Abundance (%)
623 °C					
amorphous	22.5 ± 0.2	0.02 ± 0.01		0.40	
659 °C					
amorphous	22.4 ± 0.2	0.01 ± 0.01		0.40	
paramagnetic			0.56 ± 0.04	0.7 ± 0.1	9

formation of t-Fe_3B. E_2 corresponds to a weak phenomenon extending over a large temperature range, instead of a sharp peak as usually observed for crystallization reactions, suggesting that in $Fe_{74}Dy_6B_{20}$ alloy, the formation of t-Fe_3B occurs through a progressive extension of a local order of t-Fe_3B-type already present in the initial amorphous state. As the atomic proportion of iron is about 75% in the initial amorphous alloy and in t-Fe_3B, the same proportion of iron is expected in the remaining amorphous fraction. This means that the latter is globally enriched in dysprosium and impoverished in boron. The 20 °C increase observed in the remaining amorphous fraction after the formation of t-Fe_3B cannot be explained by an increase of the ratio x_{Dy}/x_B if this remaining fraction is considered homogeneous (it could induce a Curie temperature decrease [33–36]). In contrast, if we assume that the residual amorphous is heterogeneous, the impoverishment in Dy of a fraction A_1 of it can lead to a Curie temperature increase. In this case, the complementary fraction, called A_2, is Dy enriched. The formation of t-Fe_3B thus seems to be associated with a segregation of the remaining amorphous fraction into two amorphous 'phases'. The subsequent exothermic reaction, called M_1, occurring around 589 °C, consists in the disappearance of t-Fe_3B boride. The 50 °C Curie temperature increase observed by DSC in the remaining amorphous material indicates that the segregation phenomenon goes on. After the XRD study, at 623 °C (P_1), the crystalline fraction of the sample is mainly composed of o-Fe_3B and $Dy_3Fe_{62}B_{14}$. The disappearance of t-Fe_3B is generally associated with its transformation into bcc iron and Fe_2B [5, 37]. In our alloy, the disappearance of t-Fe_3B is not due to a decomposition into bcc iron and Fe_2B as their formation is not detected by XRD or MS in this temperature range. As a consequence, our results would suggest a transformation of t-Fe_3B into o-Fe_3B during the reaction M_1. At 623 °C, we observe the crystallization of the metastable ternary compound $Dy_3Fe_{62}B_{14}$, which is impoverished in Dy and B relative to the initial amorphous alloy and is probably favoured by the Dy impoverishment in the amorphous 'phase' A_1, observed during the reactions E_2 and M_1. The crystallization of such a ternary compound has already been observed in alloys with close compositions ($\approx Fe_{77}R_{3.8}B_{19.2}$) and various rare earth elements [38–41].

The slight increase in the proportion of $Dy_3Fe_{62}B_{14}$ relatively to those of bcc iron and o-Fe_3B between 623 °C and 659 °C confirms that $Dy_3Fe_{62}B_{14}$ crystallization is subsequent to o-Fe_3B crystallization. At 659 °C, DSC analysis shows an important exothermic reaction,

identified by MS as the formation of an amorphous precursor for the $Dy_{1+\varepsilon}Fe_4B_4$ crystalline phase. This transformation occurs in the residual amorphous material, most probably in the fraction (A_2) progressively enriched in dysprosium at lower temperatures. The formation of such an amorphous precursor from A_2 seems to be confirmed by the subsequent crystallization of $Dy_{1+\varepsilon}Fe_4B_4$ detected by XRD during M_2 (695 °C). It may also explain the weak enthalpy variation associated with the crystallization of $Dy_{1+\varepsilon}Fe_4B_4$ phase itself. The last reaction (P_3), related to the decomposition of metastable $Dy_3Fe_{62}B_{14}$ compound, occurs at 733 °C. After our study, possible $Dy_3Fe_{62}B_{14}$ decomposition products are mainly bcc iron, $Dy_{1+\varepsilon}Fe_4B_4$ and, maybe, Fe_2B and o-Fe_3B. Simple calculations show that from strict composition considerations, the reaction

$$Dy_3Fe_{62}B_{14} \rightarrow \text{bcc iron} + Dy_{1+\varepsilon}Fe_4B_4 + Fe_2B$$

is possible, the atomic percentages of the various phases being respectively 56.3% (bcc iron), 30.1% ($Dy_{1+\varepsilon}Fe_4B_4$) and 13.6% ($Fe_2B$). This is also the case for the reaction

$$Dy_3Fe_{62}B_{14} \rightarrow \text{bcc iron} + Dy_{1+\varepsilon}Fe_4B_4 + Fe_3B$$

with respective proportions of 51.8, 30.1 and 18.1%. Our results rather favour the second decomposition scheme, but Fe_2B is probably also present as traces. In the sample heated up to 800 °C, the proportions of the various phases, calculated after Mössbauer abundances, are 49% for bcc iron, 40% for $Dy_{1+\varepsilon}Fe_4B_4$ and 11% for o-Fe_3B.

5. Crystallization of $Fe_{70}Dy_{10}B_{20}$

5.1. Calorimetric investigation

5.1.1. Heating up to 800 °C. For an identical thermal treatment as in 4.1.1, the calorimetric behaviour of $Fe_{70}Dy_{10}B_{20}$ alloy differs from that of $Fe_{74}Dy_6B_{20}$ as only two sharp exothermic peaks are observed at 608 °C (S_1) and 687 °C (S_2) for the first heating (figure 9(a)).

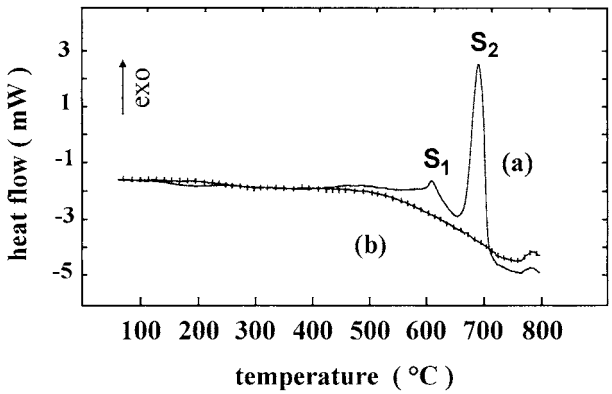

Figure 9. DSC curves of $Fe_{70}Dy_{10}B_{20}$ up to 800 °C, with a heating rate of 5 °C min^{-1}. Curves (a) and (b) are related respectively to the first and the second heating stages.

5.1.2. Successive treatments. Only one series of treatments will be detailed (figure 10).

First the sample was heated twice up to 400 °C. Both recorded DSC curves (figures 10(a) and 10(b)) exhibit a wide minimum at 196 °C, corresponding to the Curie temperature T_C^{am} of the ribbons [14]. An exothermic reaction (R_1), similar to the one (E_1) observed for $Fe_{74}Dy_6B_{20}$

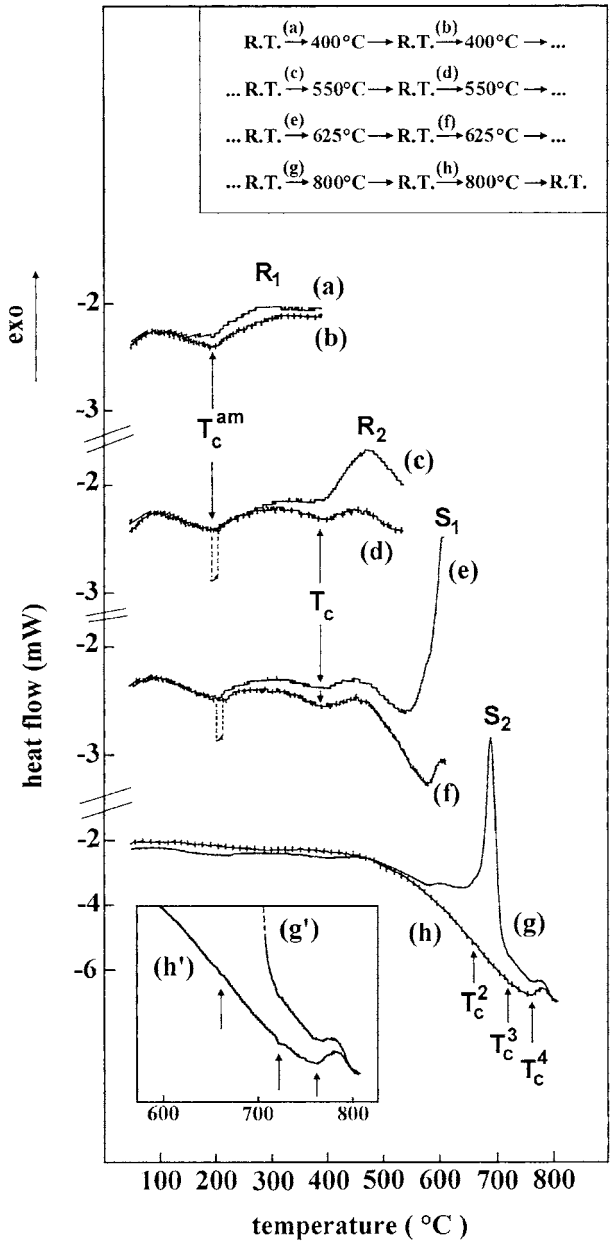

Figure 10. DSC scans obtained for successive thermal treatments on $Fe_{70}Dy_{10}B_{20}$. (g′) and (h′): expanded view of curves (g) and (h) in the temperature range 600–800 °C.

alloy, is attributed to a structural relaxation of the amorphous state. Like E_1, R_1 does not induce any significant variation of the Curie temperature T_C^{am} of the amorphous alloy. The enthalpy variation $\Delta H(R_1)$ associated with this relaxation was estimated as 0.9 ± 0.3 kJ mol^{-1}. Curve 10(c), recorded on further heating of the sample up to 550 °C, is identical to curve 10(b) in the temperature range $T \leqslant 400$ °C. An exothermic reaction (R_2) is observed at higher

temperatures, of which the maximum is located at 477 °C. It is at the origin of the 10 °C increase of the Curie temperature T_C^{am}, detected on the second heating up to 550 °C (figure 10(d)). As an extra magnetic transition T_C is observed at 393 °C on curve (d), R_2 results either from a segregation of the amorphous alloy into several amorphous 'phases' or from the formation of a crystalline compound. It could not be identified up to this stage of our study.

After cooling to RT, the sample was treated up to 625 °C (figure 10(e)), and the two magnetic transitions previously observed (T_C^{am} and T_C) take place again. The reaction S_1 of figure 9(a) is initiated, while the direct thermal treatments up to 800 °C suggested that this reaction was completed at 625 °C. For this sample, the previous heating stages tend to delay the subsequent reactions, a behaviour which is opposite to the one observed in $Fe_{74}Dy_6B_{20}$ alloy. Like R_2, S_1 is responsible for structural modifications of the amorphous state, leading again to a 10 °C shift of the magnetic transition T_C^{am} towards higher temperatures (figure 10(f)).

The sample was finally heated up to 800 °C (figure 10(g)). The expected reaction (S_2) is preceded by what seems to be a residue of S_1. As in $Fe_{74}Dy_6B_{20}$, o-Fe_3B, Fe_2B and bcc iron seem present among the final crystallization products of this sample. They are characterized by their magnetic transitions on curve 10(h). On this curve, the magnetic transition T_C^{am} of the amorphous fraction and the one (T_C) previously observed at 393 °C are no longer detected, indicating that the phase concerned by the latter Curie temperature is metastable, like the initial amorphous phase.

5.2. Characterization of the crystallization products

XRD patterns and Mössbauer spectra were recorded at room temperature for various samples heated once up to temperatures T_m, with temperatures T_m chosen at 375 and 575 °C for the lower temperature range, 625 and 650 °C for the identification of S_1 and finally 675, 700 and 800 °C for S_2.

5.2.1. Structural evolution. The XRD patterns of the samples heated up to temperatures T_m in the range 375–650 °C evolve quite continuously (figure 11). The enhancement of bcc iron (110) and (200) lines indicates a progressive crystallization of iron in the whole range explored, probably through the growth of the Fe crystallites formed on powdering.

The XRD pattern obtained at 375 °C only slightly differs from the untreated powder case, confirming the DSC results. At 575 °C, the main contribution to the pattern becomes more asymmetrical. The deformation is due to an increase of the low 2θ value contributions, suggesting the formation of extra Fe–Dy pairs. The asymmetry effect is enhanced at 625 °C and new sharp lines appear as well as two maxima in the range 65–75° (marked by arrows in figure 11). These features are enhanced on the pattern obtained at 650 °C. The sharp lines correspond to the most intense $Dy_{1+\varepsilon}Fe_4B_4$ lines.

In agreement with the XRD results, the evolution of the Mössbauer spectra is continuous in the range 375–650 °C (figure 12). We observe an increase of the intensity of the typical bcc-iron sextet, detected on all spectra since 375 °C. According to XRD results, the samples heated up to 375 and 575 °C are composed of an amorphous phase, which is the main component, and bcc iron. The spectra were thus fitted with a bcc-iron component and a distribution of hyperfine parameters (figure 12(A) and (B)). At 375 °C, the Mössbauer abundance of bcc iron is about 2% (table 3). The evolution of the amorphous fraction seems weak between the two temperatures. However, as T_m increases, the maximum of the hyperfine fields distribution shifts of about 0.5 T towards higher fields. The shift is not global and the distribution is subjected to a deformation, with a widening around the maximum. As the deformation is probably related to the appearance of the two maxima around 65–75° in the corresponding XRD pattern (figure 11), the spectrum

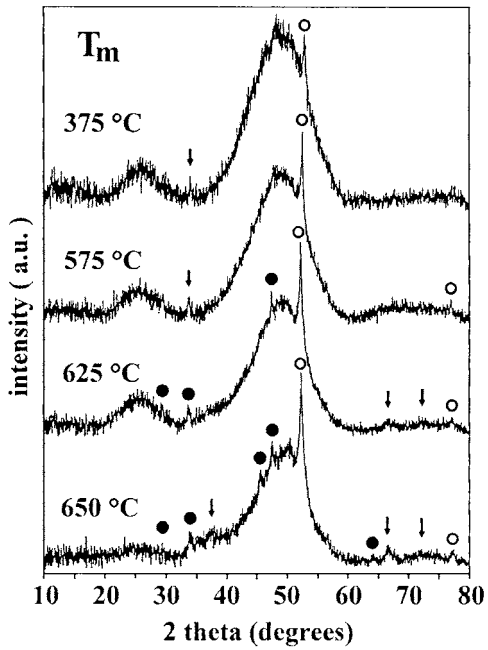

Figure 11. Room temperature XRD patterns of $Fe_{70}Dy_{10}B_{20}$ after thermal treatments up to T_m. (○): bcc iron; (●): $Dy_{1+\varepsilon}Fe_4B_4$.

Table 3. Room temperature hyperfine parameters of $Fe_{70}Dy_{10}B_{20}$ components after treatments up to T_m in the range 375–650 °C.

Component	B_{hf} (T)	IS (mm s^{-1})	QS or 2ε (mm s^{-1})	Γ (mm s^{-1})	Abundance (%)
375 °C					
amorphous	18.0 ± 0.2	-0.02 ± 0.01	0	0.40	
bcc iron	32.7 ± 0.6	-0.01 ± 0.02	0	0.4 ± 0.2	2
575 °C					
amorphous	18.2 ± 0.2	-0.00 ± 0.01	0	0.40	
bcc iron	32.9 ± 0.2	0.01 ± 0.02	0	0.26 ± 0.06	4
625 °C					
amorphous	19.2 ± 0.2	-0.02 ± 0.01	0	0.40	89
bcc iron	33.2 ± 0.2	0.02 ± 0.02	0	0.32 ± 0.06	5
iron boride	23.7 ± 0.2	0.16 ± 0.04	-0.08 ± 0.05	0.40	6
650 °C					
amorphous	20.7 ± 0.2	-0.02 ± 0.01	0	0.40	83
bcc iron	32.9 ± 0.2	0.00 ± 0.01	0	0.25 ± 0.04	7
iron boride	23.4 ± 0.2	0.14 ± 0.03	0.00 ± 0.03	0.32 ± 0.08	8
$Dy_{1+\varepsilon}Fe_4B_4$	—	0.014	0.532	0.22 ± 0.08	1

at 625 °C was fitted with an extra crystalline contribution (figure 12(C)). The hyperfine field distribution no longer exhibits the deformation and B_{hf} amounts to 23.7 ± 0.2 T for the extra contribution (table 4), which is typical of iron borides [28]. If the presence of iron borides is demonstrated at 625 °C, our Mössbauer study does not allow us to distinguish among the various forms of Fe–B compounds.

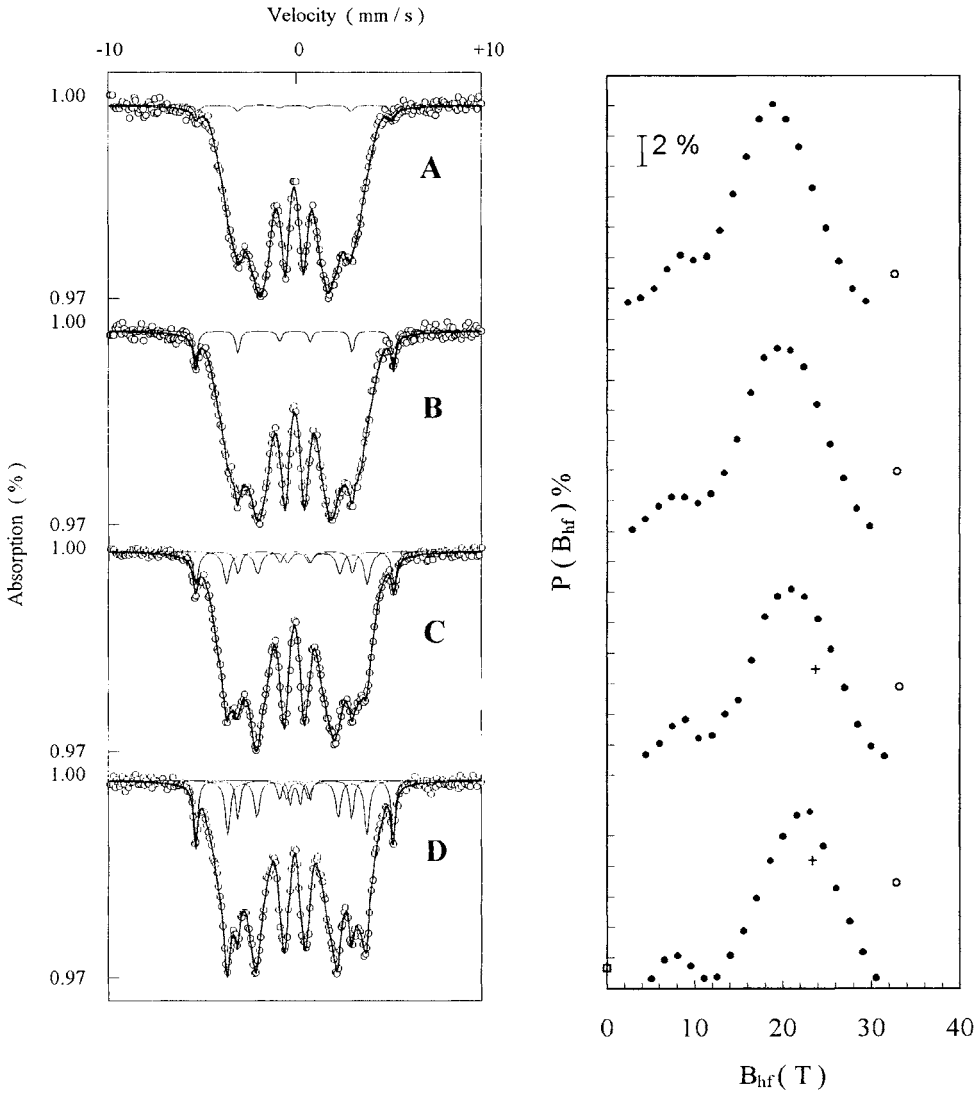

Figure 12. Room temperature Mössbauer spectra of $Fe_{70}Dy_{10}B_{20}$ after thermal treatments up to 375 °C (A), 575 °C (B), 625 °C (C) and 650 °C (D). Extra crystalline components (□): paramagnetic, (○): bcc iron, (+): iron boride.

In agreement with the XRD results, the features of the Mössbauer spectrum are more pronounced at 650 °C (figure 12(D)) than at 625 °C (C). Spectrum (D) was thus fitted as previously, with an extra paramagnetic component accounting for the very weak widening of the central lines (table 3). The parameters of the paramagnetic contribution were constrained to those of $Dy_{1+\varepsilon}Fe_4B_4$, which the crystallization is detected by XRD at this temperature (figure 11). The $Dy_{1+\varepsilon}Fe_4B_4$ accounting for the widening of the central lines has a Mössbauer abundance (about 1%) close to the detectability threshold. The fitting results confirm the increase of bcc-iron and boride(s) crystalline fractions. The hyperfine parameters of the two contributions agree within fitting accuracy with those obtained at 625 °C.

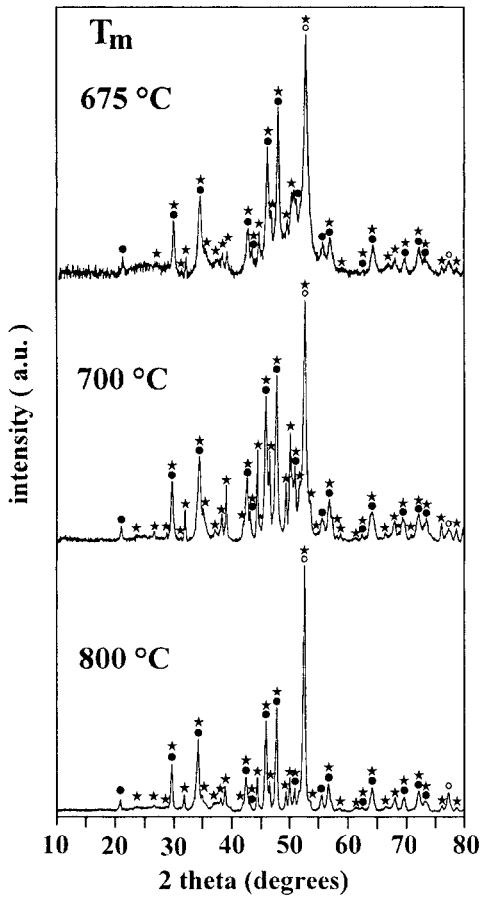

Figure 13. Room temperature XRD patterns of $Fe_{70}Dy_{10}B_{20}$ after thermal treatments up to T_m. (○): bcc iron; (●): $Dy_{1+\varepsilon}Fe_4B_4$; (*): $Dy_2Fe_{14}B$.

Above 675 °C, the shape of the XRD patterns changes drastically (figure 13), and numerous lines appear. They become sharper when the temperature increases. These lines can be attributed to the crystallization of bcc iron, $Dy_{1+\varepsilon}Fe_4B_4$ and $Dy_2Fe_{14}B$. For the latter, experimental *d*-spacings agree with those calculated after [42] using the lattice parameters taken from [43]. The intensity of bcc-iron lines increases relative to those of $Dy_{1+\varepsilon}Fe_4B_4$ between 700 and 800 °C.

The Mössbauer spectrum corresponding to the treatment up to 800 °C is displayed in figure 14. After the previous study, once crystallized, the alloy is a mixing of the crystalline phases bcc iron, $Dy_{1+\varepsilon}Fe_4B_4$ and $Dy_2Fe_{14}B$, as well as iron borides. Orthorhombic Fe_3B boride is the most probable owing to the results obtained up to this stage. Provided the complexity of the spectrum, the intensity ratios of $Dy_2Fe_{14}B$ sextets were constrained to the site occupancies. The fitted hyperfine parameters (table 4) are in very good agreement with the values published for the various phases [44]. Atomic percentages of each phase were estimated from Mössbauer abundances, assuming an identical resonant absorption cross section for all sites. We obtained respectively 30% (bcc iron), 38% ($Dy_{1+\varepsilon}Fe_4B_4$), 21% ($Dy_2Fe_{14}B$) and 9% (o-$Fe_3B$). This globally corresponds to an alloy with composition $Fe_{70.5}Dy_{7.3}B_{20.1}$. It is noteworthy that two

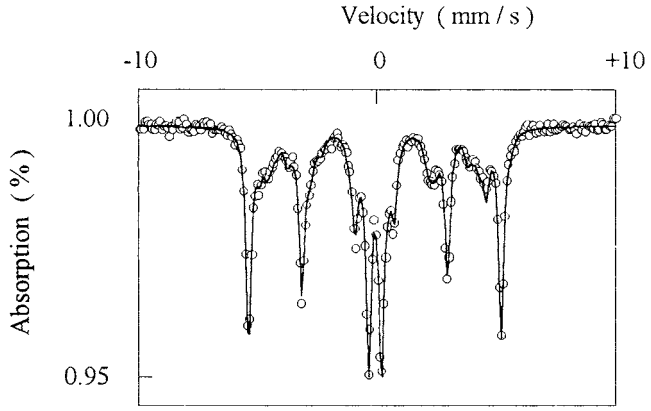

Figure 14. Fitting of the room temperature Mössbauer spectrum of $Fe_{70}Dy_{10}B_{20}$ after a thermal treatment up to 800 °C.

Table 4. Room temperature hyperfine parameters of $Fe_{70}Dy_{10}B_{20}$ after a treatment up to 800 °C.

Component	B_{hf} (T)	IS (mm s^{-1})	QS or 2ε (mm s^{-1})	Γ (mm s^{-1})	Abundance (%)
bcc iron	33.1 ± 0.2	0.005 ± 0.004	0	0.26 ± 0.01	42
$Dy_{1+\varepsilon}Fe_4B_4$	—	0.019 ± 0.004	0.52 ± 0.01	0.27 ± 0.01	24
$Dy_2Fe_{14}B$					
$16k_1$	28.9 ± 0.5	0.00 ± 0.03	0.13 ± 0.06	0.32	7.2
$16k_2$	29.8 ± 0.4	-0.18 ± 0.03	0.23 ± 0.06	0.32	7.2
$8j_1$	27.2 ± 0.9	-0.10 ± 0.06	0.25 ± 0.10	0.32	3.6
$8j_2$	34.7 ± 0.8	-0.04 ± 0.06	0.42 ± 0.11	0.32	3.6
4e	28.4 ± 1.5	-0.06 ± 0.10	-0.63 ± 0.22	0.32	1.8
4c	26.7 ± 1.5	-0.15 ± 0.10	0.0 ± 0.2	0.32	1.8
o-Fe_3B	26.6 ± 1.0	0.02 ± 0.7	0.29 ± 0.13	0.32	3
	23.7 ± 0.4	0.05 ± 0.03	0.13 ± 0.06	0.32	6

dysprosium atoms are lacking, suggesting the presence of a weak fraction of pure dysprosium or, more probably, Dy_2O_3 oxides in the alloy.

5.3. Discussion

The first exothermic phenomenon we observe is a weak reaction R_1, spreading over a large temperature range and corresponding to a structural relaxation of the material.

After the DSC study, a metastable compound or an amorphous phase with a Curie temperature T_C of 393 °C is formed during the next exothermic reaction (R_2). No crystalline compound, except bcc iron, is detected by XRD or MS at 575 °C. As a consequence, segregation phenomena have to be invoked and the magnetic transition T_C has to be attributed to a second amorphous fraction (B_2) of the alloy. From the comparison of its Curie temperature with those of $Fe_{80-x}Dy_xB_{20}$ ribbons [14], it may correspond to an amorphous phase with a dysprosium concentration close to zero. The formation of such an amorphous 'phase' (with composition close to $Fe_{80}B_{20}$), leading to a greater variety of iron environments in the sample, may explain the widening of the hyperfine field distribution observed at 575 °C (figure 12(B)). However, it does not explain the increase of the Curie temperature of the 'initial' amorphous fraction for the reasons already detailed in the case of $Fe_{74}Dy_6B_{20}$ alloy. To account for this variation,

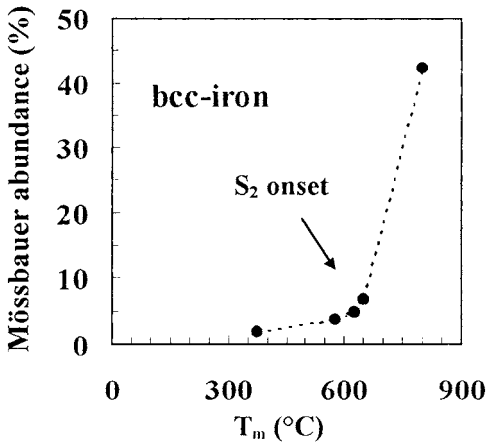

Figure 15. Evolution of bcc iron Mössbauer abundance in $Fe_{70}Dy_{10}B_{20}$ as a function of T_m.

it is again necessary to admit the existence of a third amorphous phase, named B_3, with an increasing rare earth content. It may be at the origin of the enhancement of the Dy–Dy correlations observed in the XRD patterns (figure 11).

Subsequently to the segregation of the initial amorphous alloy into three amorphous phases, named respectively B_1, B_2 and B_3, we observe the exothermic reaction S_1. The analysis of the XRD patterns recorded at 625 and 650 °C mainly evidences for the beginning of the crystallization of the paramagnetic phase $Dy_{1+\varepsilon}Fe_4B_4$. This crystalline compound is detectable by Mössbauer spectrometry at 650 °C (figure 12(D)). The $Dy_{1+\varepsilon}Fe_4B_4$ compound probably originates from the 'third' amorphous fraction (B_3) that was enriched in Dy.

The Mössbauer study also provides evidence for the existence of a component typical of the iron borides, of which the abundance increases between 625 and 650 °C. This (or these) boride(s) probably originate(s) from the Fe–B amorphous phase with a Curie temperature T_C of 393 °C (B_2), detected by DSC. Owing to the presumed composition of B_2 (about $Fe_{80}B_{20}$), the iron boride would have a composition closer to Fe_3B than to Fe_2B. The crystallization of the Fe–B amorphous fraction into borides is not complete, as its Curie transition is still observed once S_1 is ended. After XRD and MS studies, the crystallization of bcc iron goes on in this temperature range. It is attributed to a progressive growth of the crystallites formed at the surface of the particles on powdering.

The last reaction (S_2) consists in the quasi-simultaneous crystallization of the remaining amorphous fraction into bcc iron, $Dy_{1+\varepsilon}Fe_4B_4$, $Dy_2Fe_{14}B$ and o-Fe_3B. The iron boride probably crystallizes again from the Fe–B amorphous phase. Iron crystallizes in the whole explored range but its 'volume' crystallization essentially occurs during S_2, as evidenced by the thermal evolution of its Mössbauer abundance (figure 15).

6. Conclusion

The transformation processes of $Fe_{74}Dy_6B_{20}$ and $Fe_{70}Dy_{10}B_{20}$ amorphous alloys differ for both alloy compositions. In $Fe_{74}Dy_6B_{20}$, part of the amorphous alloy crystallizes into t-Fe_3B at 450 °C. The remaining fraction is heterogeneous and consists of two amorphous 'phases'. One of them (A_1) is impoverished in rare earth, while the other (A_2) is Dy enriched. At about 590 °C, the t-Fe_3B compound disappears, leading to the formation of o-Fe_3B boride.

The progressive evolution of the amorphous phases leads to successive crystallizations of $Dy_3Fe_{62}B_{14}$ from A_1 at 623 °C and $Dy_{1+\varepsilon}Fe_4B_4$ from A_2 at 732 °C. At this temperature, the $Dy_3Fe_{62}B_{14}$ metastable compound decomposes into bcc iron, $Dy_{1+\varepsilon}Fe_4B_4$ and iron borides (mainly o-Fe_3B). The formation of t-Fe_3B iron boride appears to occur through a progressive extension of a t-Fe_3B-type short-range order already present in the amorphous state.

In $Fe_{70}Dy_{10}B_{20}$, segregation phenomena occur at 575 °C in the amorphous state, prior to any crystallization. The amorphous material appears as composed of a Dy-impoverished fraction (B_1), a Dy-enriched fraction (B_3) and a part containing mainly iron and boron (B_2). The progressive evolution of these amorphous 'phases' finally leads to the quasi-simultaneous crystallization of bcc iron, $Dy_{1+\varepsilon}Fe_4B_4$, $Dy_2Fe_{14}B$ and o-Fe_3B around 690 °C.

With the assumption of a correlation between the local structure of the amorphous state and the nature of the first crystallization product, our results on the $Fe_{74}Dy_6B_{20}$ alloy suggest the existence of local environments of t-Fe_3B type in the alloy, as in amorphous $Fe_{80}B_{20}$. The early transformation stages observed in $Fe_{70}Dy_{10}B_{20}$ are different from those deduced in $Fe_{74}Dy_6B_{20}$, and local environments seem more complex, as they probably involve dysprosium. Our study would thus tend to confirm that local environments are different on both sides of the critical rare earth concentration x_c demonstrated by our previous Mössbauer study [3].

Acknowledgments

The authors would like to thank Dr R Krishnan and Dr L Driouch from the Université de Versailles (France) for providing the samples.

References

[1] Hansen P 1991 *Handbook of Magnetic Materials* vol 6, ed K H J Buschow (Amsterdam: North-Holland–Elsevier) pp 289–452
[2] Ravach G, Fnidiki A, Teillet J, Greneche J M, Krishnan R and Lassri H 1995 *J. Magn. Magn. Mater.* **140–144** 317–18
[3] Ravach G, Teillet J, Fnidiki A, Le Breton J M, Driouch L and Hassanaïn N 1996 *J. Magn. Magn. Mater.* **157/158** 173–4
[4] Ravach G and Teillet J 1998 *J. Phys.: Condens. Matter* **10** 7065–78
[5] Kemény T, Vincze I, Fogarassy B and Arajs S 1979 *Phys. Rev.* B **20** 476–88 and references therein
[6] Zhang Y D, Budnick J I, Ford J C, Hines W A, Sanchez F H and Hasegawa R 1987 *J. Appl. Phys.* **61** 3231–3
[7] Sanchez F H, Zhang Y D, Budnick J I and Hasegawa R 1989 *J. Appl. Phys.* **66** 1671–5
[8] Schaafsma A S, Snijders H, van der Woude F, Drijvers J W and Radelaar S 1979 *Phys. Rev.* B **20** 44 236
[9] Köster U and Herold U 1981 *Glassy Metals I (Topics in Applied Physics 46)* ed H J Güntherodt and H Beck (Berlin: Springer) ch 10 and references therein
[10] Svàb E, Faigel G, Mézàros G, Ishmaev S N, Sadikov I P and Chernyshov A A 1985 *J. Physique.* **46** 267–71
[11] Teillet J and Varret F 1976 MOSFIT program
[12] Varret F 1982 *Proc. Int. Conf. on Mössbauer Effect* (New Delhi: Indian National Science Academy) pp 129–40
[13] Cullity B D 1978 *Elements of X-Ray Diffraction* 2nd edn (Reading, MA: Addison-Wesley)
[14] Driouch L 1995 *Thesis* Rouen
[15] Ravach G, Saiter J M, Fnidiki A and Teillet J 1993 *Mater. Lett.* **18** 35–8
[16] Chamberod A, Chambron W and Hillairet J 1983 *Les Amorphes Métalliques (Aussois, 1983)* (Les Ulis: Éditions de Physique) p 329
[17] Chien C L, Musser D, Gyorgy E M , Sherwood R C, Chen H S, Luborsky F and Walter J L 1979 *Phys. Rev.* B **20** 283–95
[18] Fruchart R and Michel A 1959 *Mem. Soc. Chim.* **11** 422
[19] Arajs S and Colvin R V 1964 *J. Appl. Phys.* **35** 2424
[20] Cadeville M and Meyer A J P 1962 *C. R. Acad. Sci., Paris* **255** 339
[21] de Mooij D B, Daams J L C and Buschow K H J 1987 *Philips J. Res.* **42** 339–49
[22] Withanawasam L, Hadjipanayis G C and Krause R F 1995 *Nanostructured and Non-Crystalline Materials,*

Proc. 4th Int. Workshop on Non-Crystalline Solids (1994) ed M Vazquez and A Hernando (Singapore: World Scientific) pp 311–24
[23] Herold U and Köster U 1978 *Z. Metallkde* **69** 326–32
[24] Khan Y, Kneller E and Sostarich M 1982 *Z. Metallkde* **73** 624–6
[25] Bezinge A, Braun H F, Muller J and Yvon K 1985 *Solid State Commun.* **55** 131–5
[26] Niarchos D, Zouganelis G, Kostikas A and Simopoulos A 1986 *Solid State Commun.* **59** 389–91
[27] Visser J 1984 *JCPDS Grant-in-Aid Report* 36-1332 Technisch Physische Dienst, Delft
[28] Dubois J M 1981 *Thesis* Nancy
[29] Choo W K and Kaplow R 1977 *Metall. Trans.* A **8** 417
[30] Weisman I D, Swartzzendruber L J and Bennett L H 1969 *Phys. Rev.* **177** 465–71
[31] Murphy K A and Hershkowitz N 1973 *Phys. Rev.* B **7** 23–31
[32] Greer A L and Leake J A 1979 *J. Non-Cryst. Solids* **33** 291–7
[33] Gu B X, Zhai H R and Shen B G 1990 *Phys. Rev.* B **42** 10 648–52
[34] Yang L Y, Shen B G, Zhang J X, Wo F, Ning T S, Zhao J G, Guo H Q and Zhan W S 1990 *J. Less-Common Met.* **166** 189–93
[35] Miyazaki T, Takada H and Takahashi M 1987 *Phys. Status Solidi* a **99** 611–18
[36] Teillet J, Lassri H, Krishnan R and Laggoun A 1990 *Hyperfine Interact.* **55** 1083–8
[37] Takahashi M, Koshimura M and Abuzuka T 1981 *Japan. J. Appl. Phys.* **20** 1821–32
[38] Coehoorn R and De Waard C 1990 *J. Magn. Magn. Mater.* **83** 228–30
[39] Cheng Z H, Mao M X, Sun J J, Shen B G, Wang F W, Yang C L, Zhang Y D and Li F S 1995 *J. Phys.: Condens. Matter* **7** 2303–12
[40] Altounian Z, Ryan D H and Tu G H 1988 *J. Appl. Phys.* **64** 5723–5
[41] Liao L X and Altounian Z 1989 *J. Appl. Phys.* **66** 768–71
[42] Herbst J F, Croat J J, Pinkerton F E and Yelon W B 1984 *Phys. Rev.* B **29** 4176
[43] Fruchart R *et al* 1987 *J. Phys. F: Met. Phys.* **17** 483–501
[44] Van Noort H M, de Mooij D B and Buschow K H J 1986 *J. Less-Common Met.* **115** 155–65